AIP Advances

In vitro characterization of Lagrangian fluid transport downstream of a dysfunctional bileaflet mechanical aortic valve

Cite as: AIP Advances **10**, 095319 (2020); https://doi.org/10.1063/5.0021372
Submitted: 10 July 2020 • Accepted: 01 September 2020 • Published Online: 21 September 2020

Ahmed Darwish, Giuseppe Di Labbio, Wael Saleh, et al.

COLLECTIONS

Paper published as part of the special topic on Mathematical Physics

View Online Export Citation CrossMark

ARTICLES YOU MAY BE INTERESTED IN

Reduced-order modeling of left ventricular flow subject to aortic valve regurgitation
Physics of Fluids **31**, 031901 (2019); https://doi.org/10.1063/1.5083054

Pulsatile twin parallel jets through a flexible orifice with application to edge-to-edge mitral valve repair
Physics of Fluids **32**, 121702 (2020); https://doi.org/10.1063/5.0025859

Transitions between systems of satellite vortices in a rotating fluid
Physics of Fluids **32**, 101701 (2020); https://doi.org/10.1063/5.0025030

© 2020 Author(s).

In vitro characterization of Lagrangian fluid transport downstream of a dysfunctional bileaflet mechanical aortic valve

Cite as: AIP Advances 10, 095319 (2020); doi: 10.1063/5.0021372
Submitted: 10 July 2020 • Accepted: 1 September 2020 •
Published Online: 21 September 2020

View Online Export Citation CrossMark

Ahmed Darwish,[1,a),b)] Giuseppe Di Labbio,[2] Wael Saleh,[1,b)] and Lyes Kadem[1]

AFFILIATIONS

[1] Laboratory of Cardiovascular Fluid Dynamics, Concordia University, Montréal, Quebec H3G 1M8, Canada
[2] Laboratoire de Dynamiques des Fluides, Polytechnique Montréal, Montréal, Quebec H3C 3A7, Canada

[a)] **Author to whom correspondence should be addressed:** lcfd@encs.concordia.ca
[b)] **Also at:** Mechanical Engineering Department, Assiut University, 71515, Egypt.

ABSTRACT

This experimental study aims to explore the Lagrangian nature of fluid transport downstream of a bileaflet mechanical aortic valve under different malfunction scenarios that might be encountered clinically. Time-resolved planar particle image velocimetry measurements are performed to extract instantaneous velocity fields downstream of the bileaflet mechanical valve implanted in an elastic aortic model. The results show an increase in particle residence time with the severity of malfunction. This is attributed to the expansion of the recirculation regions downstream of the valve. The time-evolution of Lagrangian coherent structures over one cardiac cycle (using finite-time Lyapunov exponent fields) shows the effect of valve dysfunction on the material transport and its barriers inside the aorta. The unbalanced flow through the dysfunctional leaflets leads to a significant redistribution of the LCS, thus the fluid transport along the ascending aorta. Moreover, a new technique for the evaluation of the highest accumulated shear stresses is applied along the Lagrangian trajectory of particles being released from the extracted Lagrangian coherent structures where the highest stretching occurs. Finally, the induced non-laminar flow behavior by the valve dysfunction is analyzed using the time-frequency spectra of velocity signals at selected points in the ascending aorta.

© 2020 Author(s). All article content, except where otherwise noted, is licensed under a Creative Commons Attribution (CC BY) license (http://creativecommons.org/licenses/by/4.0/). https://doi.org/10.1063/5.0021372

I. INTRODUCTION

The aorta is the largest artery that carries the main blood supply in our body. It is connected to the left ventricle through a native valve called the aortic valve (AV). Three leaflets form the AV where their arrangement allows for a one-way flow from the left ventricle to the ascending aorta. A known disease that affects the aortic valve is aortic stenosis (AS). It can be congenital (bicuspid valve) or acquired due to a degenerative process.[1] Moderate to severe AS has age-related prevalence ranging from 0.02% (in young patients) to 2.8% (in older patients).[2] In the presence of AS, left ventricular afterload increases causing a progressive effect on the left ventricle from hypertrophy to systolic and diastolic dysfunction.[3] In patients with severe symptomatic AS, the recommended management technique is aortic valve replacement where a prosthetic valve is used to replace the native valve.[4] The valve type can be either biological or mechanical where each one has its pros and cons. The bileaflet mechanical aortic valve (BMAV) is the most known mechanical valve and is highly recommended for young patients (<65 years old) due to its longer durability in contrast to the bioprosthetic valves.[5,6] Usually, BMAV replacement requires lifelong anticoagulation therapy in order to avoid thromboembolic events.[7] However, thrombosis can still occur with a rate varying between 0.7% and 6%.[8,9] Another complication that appears with BMAVs is pannus formation around the suture location.[10] Both thrombosis and pannus formation can restrict the movement of the leaflets causing a significant disturbance to the flow inside the ascending aorta.[10] Many previous studies, including our own, investigated the flow in the ascending aorta with a normal or dysfunctional BMAV.[11–18] Bluestein *et al.*[11] noticed a relation between the vortex shedding and the elevated shear stress

© Author(s) 2020

in the wake of a normally operating BMAV, suggesting a propensity for platelet activation. According to their study, the trajectories of platelets become longer within the wake region leading to a larger harvest of shear stresses. Moreover, they observed a phenomenon called *vortex pairing*,[19] where adjacent vortices combine to form a larger vortical structure that brings activated platelets together.[11] Bluestein *et al.*[20] reported the shear stress induced on the platelets when the valve is tilted relative to the aortic root. They noticed that the platelets near the leaflets can be activated within only one cardiac cycle.[20] This happens as a result of the high level of deformation stresses, which is caused by the high acceleration of the jet and a sudden deceleration in the wake.[20] Min Yun *et al.*[21] noticed that a high probability of platelet damage can occur in recirculation regions; therefore, they recommended studying the blood damage by focusing on high flow mixing zones. As one might expect, in the case of leaflet dysfunction, velocity magnitudes in the ascending aorta downstream of the free moving leaflet increase significantly exceeding the normal expected values.[12,18] Moreover, with an increasing degree of dysfunction, the vortical structures downstream of the valve occupy a larger area in the ascending aorta,[12] which can also promote platelet aggregation.[11]

As most of previous studies rely on Eulerian parameters to investigate the flow downstream of a BMAV, the reader may question the need to perform analyses from a Lagrangian perspective. In fluid mechanics, Eulerian analyses are not always the best approach when identifying the complexity of a flow. For instance, Cucitore *et al.*[22] demonstrated that using the velocity gradient tensor alone (an Eulerian parameter) makes it difficult to relate the behavior of two fluid elements located within a certain spatial extension of a vortex. Moreover, according to Provenzale,[23] particle trajectories in time-dependent flows may become chaotic in the Lagrangian perspective, even though the Eulerian dynamics appear to be simple. Consequently, extra caution is required when analyzing the flow characteristics from an Eulerian perspective when a Lagrangian analysis is more appropriate. This includes, for example, flow recirculation, separation, and stagnation in the cardiovascular system.[24]

In view of these points, the importance of identifying Lagrangian coherent structures (LCSs) in the cardiovascular system has attracted many investigations.[25–30] A precise definition of LCSs can provide a description of fluid transport by highlighting robust material boundaries that separate distinct fluid dynamics. As such, LCSs can provide a better understanding of the unsteady hemodynamics in cardiovascular flows. For instance, Shadden *et al.*[31] used LCSs to analyze the aortic flow using a multidimensional FSI model of a stenotic aortic valve. They noticed that LCSs can present an accurate measure of the aortic jet area for clinical assessment of aortic stenosis.

Arzani and Shadden[32] described the fluid transport inside abdominal aortic aneurysms (AAAs) using FTLEs where they described separation regions, transport of coherent vortices, mixing regions, and the jet impingement on the aortic wall. They noticed that the exact location of separation and precise delineation boundary of vortices are better-described using LCSs, while the ability of instantaneous velocity fields to distinguish such phenomena was questionable.[32]

Di Labbio *et al.*[33] investigated the left ventricular flow in the presence of aortic regurgitation. They found that left ventricular flow displays persistent attracting LCSs, which could present a favorable environment for platelet activation and agglomeration, especially for particles with long residence times. Joly *et al.*[29] investigated the stagnation regions inside AAAs using LCSs where they suggested tracking the progression of stagnation zones inside AAAs to predict their growth and rupture. Olcay *et al.*[28] investigated a stenotic aortic jet using LCSs. They showed the difference between organized vortex boundaries in the case of normal native valve leaflets and destructed vortex boundaries in the case of moderate and severe stenotic valves. Badas *et al.*[26] used LCSs to investigate the flow inside three different cases of left ventricular flows: healthy, dilated, and with a mitral mechanical valve. They considered three-dimensional finite-time Lyapunov exponent (FTLE) fields where they noticed significant differences in left ventricular LCS patterns between the healthy and mitral mechanical valve cases. Interestingly, they found an increase in stagnation regions in the case of the dilated ventricle. Overall, they used FTLE to characterize the mixing inside the left ventricle under various physiological conditions. Finally, Shadden and Hendabadi[34] noticed that in a stenotic vessel, higher platelet activation potential is maximized along the repelling LCSs.

As discussed above, FTLE fields were used extensively in a variety of cardiovascular flows. However, LCSs have not been used to investigate the flow downstream of a mechanical aortic valve, except for the work of Miron *et al.*[35] In their study, they used LCSs to analyze the wakes that develop downstream of a BMAV. Their study was limited to a normally functioning BMAV in a rigid aorta without the sinuses of Valsalva. Nevertheless, their approach combining FTLEs and time-frequency spectra allowed for an in-depth investigation of the flow in terms of development of the vortex streets and their shedding frequency.

To the best of our knowledge, no previous study has investigated LCSs in an anatomically correct ascending aorta downstream of normal and dysfunctional bileaflet mechanical valves. In this contribution, we identify attracting and repelling LCSs and their role in the accumulation of shear stresses and risks of platelet activations. We also investigate the effect of BMAV dysfunction on the particle residence time (PRT) and turbulence and intermittency generation in the ascending aorta. The rest of this paper is structured as follows: we present our experimental setup and describe our methodology including the calculation of particle residence time and the extraction of LCSs and time-frequency spectra from the time-resolved velocity fields (Sec. II); we then present our results and how BMAV dysfunction significantly impacts the flow characteristics in the ascending aorta (Sec. III). Finally, we provide a short discussion and conclusion (Sec. IV) of our results and the main limitations (Sec. V) associated with our study.

II. METHODS

A. Experimental setup

An in-house double activation left heart duplicator is used to generate physiological flow conditions inside the left heart. The duplicator has elastic left heart chambers including the left atrium, the left ventricle, and the aorta. The three chambers are made of transparent silicone (XIAMETER RTV-4234-T4) by brush-coating on 3D printed models of the heart chambers. The wall thickness along the aortic silicone mold varies between 2.53 mm for the

© Author(s) 2020

straight part and 1.76 mm at the sinus region. The silicone has a tensile strength of 6.7 MPa, and its elongation at break is 400%. The maximum wall displacement (during experiments) is 2.35 mm, which occurs close to the sinotubular junction, while the top part of the aorta has the minimum wall displacement of 1.0 mm. A mixture of water and glycerol is used with water composing 60% of its volume. The mixture has a density of 1100 kg/m^3 and a dynamic viscosity of 0.0042 Pa s. The BMAV used in this study is a St. Jude Regent 27A-101 with an internal diameter of 24.9 mm. The valve is placed below the sinuses of Valsalva. The orientation of the leaflets relative to the sinuses follows the recommendation in Ref. 36. The duplicator relies on hydraulic activation of the left ventricle in order to generate its physiological flow waveforms. To do that, the left ventricle is enclosed in a hydraulic chamber, which is connected to a piston-cylinder arrangement. The piston moves using a linear motor (LinMot P01-37 × 120, NTI AG; Spreitenbach, Switzerland), which is controlled by means of a LabVIEW (National Instruments; Austin, TX, USA) graphical user interface. The piston moves following a waveform that induces the systolic and diastolic phases on the ventricle. A detailed description of the simulator can be found in Refs. 18 and 27. In order to match the refractive indices (RI), the aorta is placed inside an open surface chamber (made of Lucite) filled with the same water/glycerol mixture (RI = 1.39), which is very close to that of the silicone used (RI = 1.41). To reproduce different scenarios of BMAV dysfunction that can be found in patients, the BMAV leaflet movement is restricted. Six cases are investigated: normal (N), sinus leaflet partially blocked (SLP), non-sinus leaflet partially blocked (NSLP), both leaflets partially blocked (BLP), sinus leaflet totally blocked (SLT), and non-sinus leaflet totally blocked (NSLT); for a schematic, see Fig. 1. The other experimental conditions consist of cardiac output = 4.3 ± 0.12 l/min, heart rate = 70 bpm, systolic pressure = 125 ± 3 mm Hg, and diastolic pressure = 70 ± 3 mm Hg. This corresponds to a Reynolds number of 3505 and a Womersley number of 16.47. The aortic flow rate is measured using a magnetic inductive flow sensor (ProSense FMM50-102, Munich, Germany). The aortic pressure (reported in Fig. 1) is measured using a fiber optic pressure sensor (FISO FOP-M260, QC, Canada; range −300 mm Hg to 300 mm Hg; and resolution <3 mm Hg).

B. Particle image velocimetry

Planar time-resolved particle image velocimetry (TR-PIV) measurements are carried out using a double-pulsed Nd-YLF laser

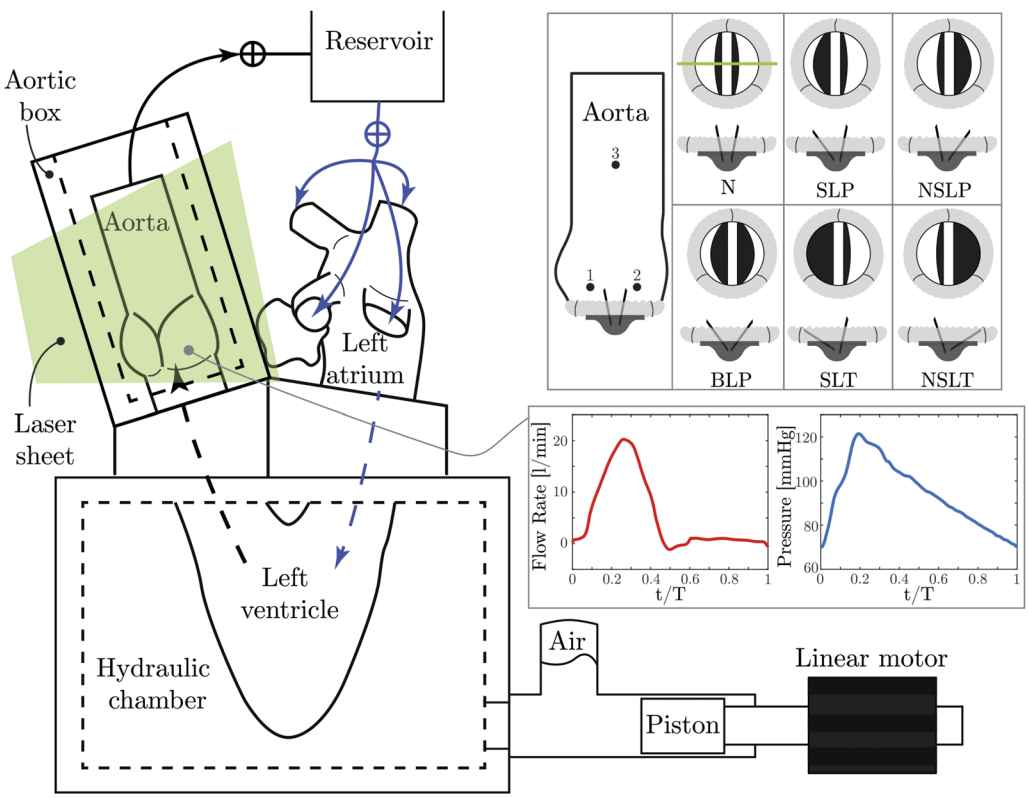

FIG. 1. Schematic of the experimental setup showing the components of the left heart duplicator and their arrangement. The left ventricle is activated using a labVIEW-controlled linear motor. On the top right, a gray border table shows a section of the aorta and the location of the mechanical valve. The maximum opening position of the leaflets is depicted for all cases where N stands for normal, SLP for sinus-side leaflet partially blocked, NSLP for non-sinus-side leaflet partially blocked, BLP for both leaflets partially blocked, SLT for sinus-side leaflet totally blocked, and NSLT for non-sinus-side leaflet totally blocked. The location of the laser sheet relative to the valve is indicated by the green line on the N case schematic. The aortic flow (red curve) and pressure (blue curve) waveforms are shown in the middle right gray cell.

© Author(s) 2020

with a 10 mJ pulse energy, a 527 nm wavelength, and a repetition rate range between 0.2 kHz and 20 kHz (LDY301, Litron Lasers; Rugby, England). The laser sheet (1 mm in thickness) is located at the center of the bileaflet mechanical heart valve normal to the leaflets, as shown in Fig. 1. The fluid inside the heart simulator is seeded with polyamide particles (with 50 μm diameter, particle settling velocity = 20 μm/s, Stokes number = $2.3 \cdot 10^{-4}$) in order to the scatter the light emitted by the laser. The images of scattered light are captured using a Phantom V9.1 high-speed camera with a frame rate of 400 fps at the full resolution of 1632 × 1200 pixels (Vision Research, Inc., Wayne, NJ, USA). Each image has two consecutive frames each capturing the effect of a laser pulse. Two time-delay values between the laser pulses are used in the experiments, where 400 μs is used with cases N, SLP, and NSLP, while 600 μs are used with cases BLP, SLT, and NSLT. The choice of the different time-delay values enhances the accuracy of the obtained velocity vectors and allows for fulfilling the 1/4 rule.[37] Post-processing of the recorded images is carried out using a multiple-pass fast Fourier transform cross-correlation with an initial 64 × 64 and a final 16 × 16 pixel^2 interrogation window with a 50% overlap. The spacing between velocity vectors is 0.55 mm. A median filter is used to remove vectors with signal-to-noise ratio <1.5. By following the guidelines in Ref. 37, the minimum confidence level in velocity fields is 95%.

C. Particle residence time (PRT)

We investigate the particle residence time (PRT) inside the ascending aorta, which is the amount of time a fluid particle will reside inside the aorta. In order to compute PRT, we construct a refined advection grid filled with massless fluid particles, then the interpolated velocity field (over the refined grid) was integrated using the fourth-order Runge–Kutta scheme to track the trajectories of the advected particles, as discussed in Ref. 38. Since the Lagrangian particle trajectories are time-dependent,[38] we computed the PRT using ten different release times,[32] equally spaced along the cardiac cycle, for all reported cases. The particles have been followed for a total of four consecutive cycles. A particle is considered to leave the domain when it reaches the boundary of the domain from any side, including the bottom, upper, and side walls. The original grid is refined 16 times where the number of advected particles is 1 917 405 ± 91 683. The dependency of the PRT value on the spatial and temporal refinement of the velocity field is tested by considering the ratio between different PRT ranges. The PRT ratio independence is achieved with grid and time refinements of 8 and 4, respectively. The adopted larger refinement ensures smoother PRT maps. To quantify the PRT variation between all cases, we computed the particle residence index (PRI).[38] The PRI is evaluated by dividing the number of remaining particles (at any time instant) by the total number of released particles. The PRI has an initial value of 1.[38]

D. Lagrangian coherent structures

According to Haller[39,40] and Shadden *et al.*[41] using FTLEs is a good approach to extract LCSs from a fluid flow. A FTLE field represents an average of the maximum expansion rate of a pair of closely adjacent particles advected in the flow. For a fluid domain with a time-dependent velocity field $\mathbf{u}(\mathbf{x}, t)$, a particle with initial location $\mathbf{x}_0$ at time t_0 is advected to follow the trajectory $\mathbf{x}(t; t_0, \mathbf{x}_0)$. A flow map $\mathcal{M}$ can be used to move the particle between different positions as follows:

$$\mathbf{x}_0 \mapsto \mathcal{M}_{t_0}^{t+\tau}(\mathbf{x}_0) = \mathbf{x}(t_0 + \tau; t_0, \mathbf{x}_0), \tag{1}$$

where τ is the time interval. Based on the explanation of Shadden *et al.*,[41] if we considered an arbitrary-oriented particle located an infinitesimal distance away $\delta\mathbf{x}(t_0)$ from the particle at $\mathbf{x}(t_0)$, the maximum stretching will happen when $\overline{\delta\mathbf{x}}(t_0)$ is aligned with the eigenvector that has a maximum eigenvalue λ_{max} of the right Cauchy–Green deformation tensor Δ,

$$\Delta_{t_0}^{t_0+\tau}(\mathbf{x}) = \left[\frac{\mathrm{d}\mathcal{M}_{t_0}^{t_0+\tau}(\mathbf{x})}{\mathrm{d}\mathbf{x}}\right]^* \left[\frac{\mathrm{d}\mathcal{M}_{t_0}^{t_0+\tau}(\mathbf{x})}{\mathrm{d}\mathbf{x}}\right], \tag{2}$$

where $[\ ]^*$ represents the transpose of matrix [ ], then

$$\max_{\delta\mathbf{x}(t_0)} \|\delta\mathbf{x}(t_0+\tau)\| = \sqrt{\lambda_{max}(\Delta(\mathbf{x}))}\,\|\overline{\delta\mathbf{x}}(t_0)\| = e^{\sigma_{t_0}^{\tau}(\mathbf{x})|\tau|}\|\overline{\delta\mathbf{x}}(t_0)\|, \tag{3}$$

$$\sigma_{t_0}^{\tau}(\mathbf{x}, t) = \frac{1}{2|\tau|}\ln\lambda_{max}(\Delta(\mathbf{x})), \tag{4}$$

where $\sigma_{t_0}^{\tau}(\mathbf{x}, t)$ is the FTLE. Therefore, FTLEs by definition can be evaluated with both negative and positive time intervals. For positive time intervals, the FTLE will measure the separation forward in time, which reveals an approximation of repelling LCSs. For negative time intervals, the FTLE will evaluate the separation of particle trajectories backward in time, which highlights attracting LCSs in forward time. To compute the FTLE fields, a grid of massless particles is advected in the flow field (as for the PRT calculation) using the fourth-order Runge–Kutta scheme with a bicubic interpolation to compute an approximation of the velocity at the new particle location. For the derivatives (which are used to compute the Cauchy–Green tensor), an explicit second-order centered finite-difference scheme is used. The value of the time interval τ for the FTLE computation is dependent on the relevant time scale of the analyzed flow.[42] Therefore, increasing τ will result in sharper FTLE lines; however, the possibility of particles leaving the flow domain for large τ should be considered. In our FTLE computations, we used a single time interval for all cases ($\tau/T = 0.17$), which is defined by the length and time scale of the investigated flow.

E. Time-frequency spectra

As the flow behind a dysfunction bileaflet mechanical heart valve (BMHV) becomes highly disturbed, we—in order to evaluate the downstream flow turbulence—performed contentious wavelet transform (CWT) analysis on velocity signals extracted at three locations of interest inside the aorta. The two velocity components (u and v) are considered in the analysis. The first two points are located above the two lateral jets; the third is located in the middle of the ascending aorta above the sinotubular junction. The three points are shown in Fig. 1. Considering the velocity component values at a certain location as our time varying signal $f(t)$, then time-frequency analysis (using continuous wavelet transform) is performed on it using a complex Morlet wavelet $\psi(t)$ [Eq. (6)] that can be shifted through the signal providing the time-localization while the scaling is used to retrieve different wavelengths scales. Both scaling and shifting parameters correspond to a and b, respectively, in Eq. (5). As such, analysis can identify turbulence in fluid mechanics;[35,43] we

© Author(s) 2020

show the velocity disturbances by displaying power intermittency at high frequencies,[43]

$$W_\psi(a,b) = \frac{1}{\sqrt{a}} \int_{-\infty}^{+\infty} f(t)\psi^*_{a,b}(t)dt, \tag{5}$$

$$\psi(t) = \pi^{-1/4} e^{i\omega_0 t} e^{-t^2/2}. \tag{6}$$

III. RESULTS

A. Retained and ejected flow

The particle residence time map was computed for all cases as reported in Sec. II. As we used ten different release times for the PRT and PRI computations, we report the PRI values by considering the PRT values from all release times. The results (in Fig. 2 and Table I) show that for all cases, the large majority (>90%) of released particles leave the ascending aorta within the first cycle. The lowest values of PRI are obtained for the N and NSLT cases with 2.87% and 3.88%, respectively. By the end of the second cycle, we can observe that only a small fraction (<1%) of the released particles remained in the ascending aorta with the most critical case being the SLT case (0.85%). Figure 9 (see the Appendix) shows an example of a PRT map with a release time at t/T = 0.49. Overall, two interesting points can be noticed from the PRT and PRI analyses: (1) the particles remaining in the ascending aorta beyond two consecutive cycles, despite their low relative percentage, have the tendency to be more localized in a region lower than one valve diameter from the valve. This is important since this may trigger thrombosis and lead to a further progression of the severity of the valve dysfunction; (2) for the same level of severity, the orientation of the dysfunctional leaflet makes a significant difference in terms of particle behaviors. If the dysfunctional leaflet is the one facing the sinus of Valsalva (SLP and SLT), then the percentage of particles retained in the ascending aorta appears to be significantly higher. Further discussion on the above-mentioned points will be addressed when presenting the FTLE fields.

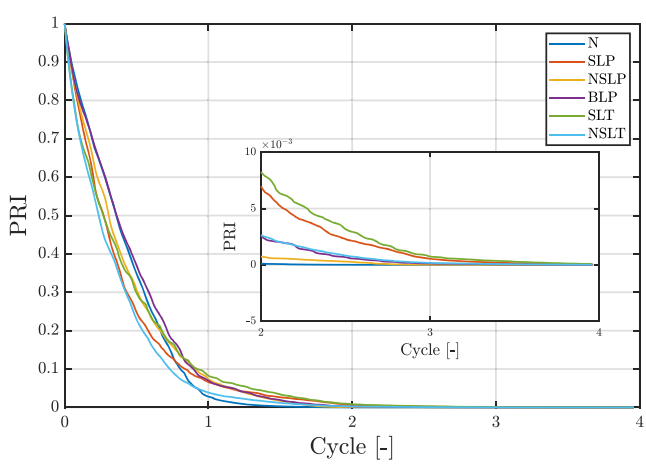

FIG. 2. Particle Residence Index (PRI) for all cases for a duration of four cardiac cycles.

TABLE I. PRI value (as a percentage) at the end of each cycle of three cardiac cycles for all cases. The values in this table represent the particles released at ten equally spaced different release times.

	PRI (%)		
Case	1st cycle	2nd cycle	3rd cycle
Normal	2.87	0.01	3.2×10^{-5}
SLP	6.67	0.73	0.0607
NSLP	7.44	0.074	0.0013
BLP	7.16	0.263	0.0123
SLT	8.40	0.85	0.0860
NSLT	3.88	0.27	0.0193

B. FTLE fields

Attracting LCSs can be revealed by conceptually injecting dye in the flow, which makes them less abstract when compared to the repelling LCSs. Figure 3 shows the backward FTLE fields in the aorta at four selected time instants during the systolic phase (t/T = 0.2, 0.27, 0.34, and 0.4). Under normal valve operation, an early formation of two mushroom-like structures (considering a planar view) at the front of each lateral jet can be noticed. The formation of these structures is attributed to the penetrating lateral jets that are oriented toward the large sinus wall during early systole. As the lateral jets propagate through the valve opening, two counter rotating vortices are formed at each jet front due to the shear-layer roll-up at the inlet boundary. Moreover, the upper part of the two mushroom-like structures has a dark spiral inside the vortical structures, which reflects the entrainment of the surrounding fluid (above the leaflets), as noted in Ref. 44. Noticeably, the jets are tilted toward the aortic wall (at instant 1). As the structures propagate in the aorta (at instant 2), the mushroom-like structures are separated where the top vortices are convected downstream for a short period without significant deformation before being dissipated [see instant 2 and Video 1 in Fig. 3 (Multimedia view)]. Furthermore, the bottom vortical structures expand to fill a relatively large area at the sinus region causing the ejected jets to slightly converge toward the center of the aorta. Moreover, instant 1 [see also Video 1 in Fig. 3 (Multimedia view) at t/T = 0.15–0.2] shows that the sinus captures a part of the vortex while the side that has no sinus seems to partly degrade the vortex. This shows the effect of the sinuses on the flow structure. As the structures propagate further downstream, they start fading (instant 3). The width of the jet boundary at the aortic root and at the sinotubular junction witnesses episodes of narrowing and expanding with time (see instants 2, 3, and 4 in Fig. 3), which points to the leaflets dynamics during their opening and closure. The reader can verify these episodes by playing Video 1 in Fig. 3 (Multimedia view) (during cardiac time t/T = 0.22–0.41). As the flow decelerates (at instant 4), a deformed vortical structure expands along the sinus region causing the sinus washout and contributing to leaflet complete closure as in Video 1 in Fig. 3 (Multimedia view) (during cardiac time t/T = 0.41–0.58).

By applying partial dysfunction on one leaflet, the LCSs that define the jet boundaries lose their organized shape due to the imbalanced flow through the leaflets, where no clear mushroom-like

© Author(s) 2020

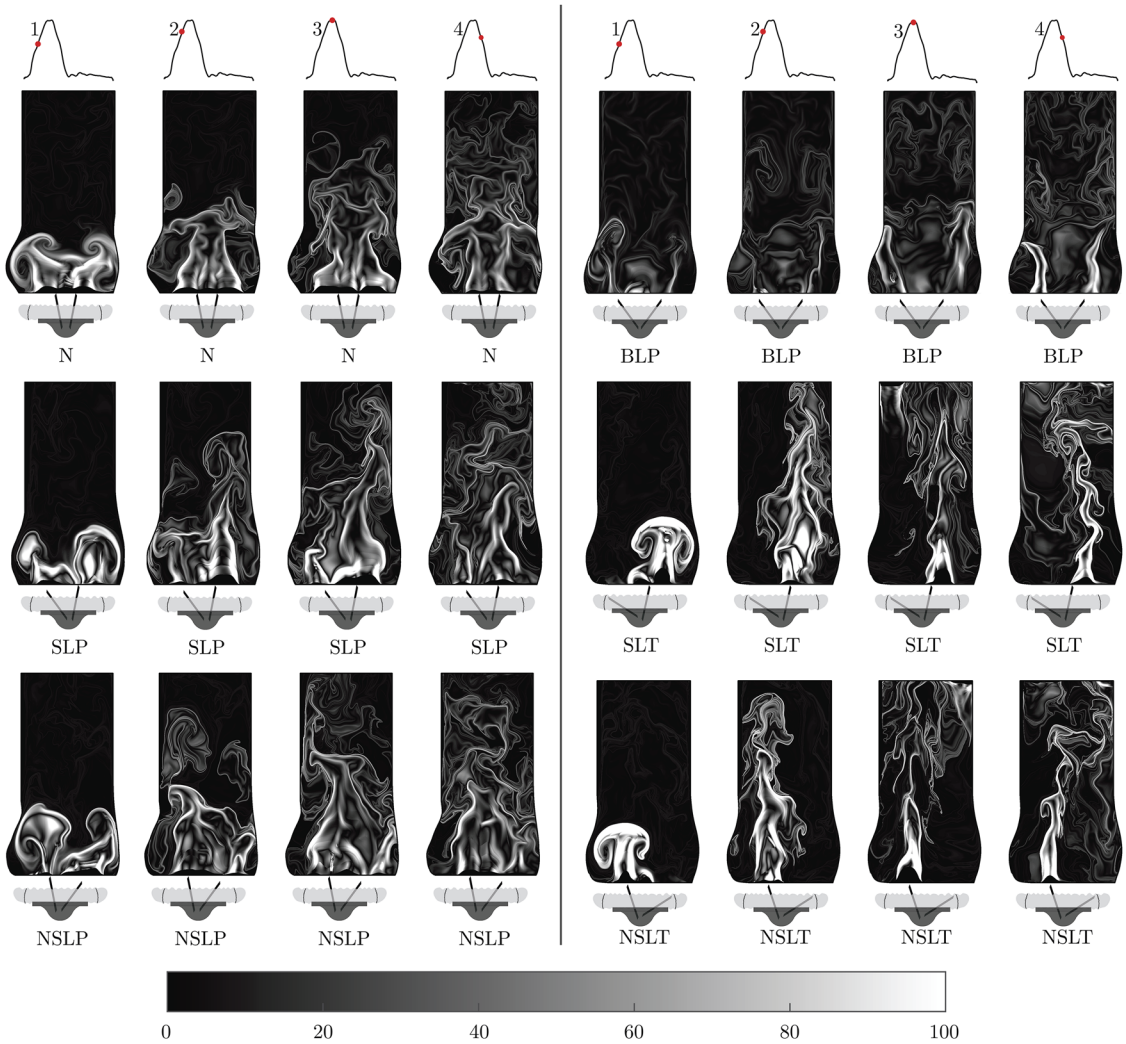

FIG. 3. Backward finite-time Lyapunov exponent fields at four time instants during the systolic phase. Inset in the top left panel shows the location of the four time instants during the cardiac cycle [instants from (1) to (4) correspond to t/T = 0.2, 0.27, 0.34, and 0.4, respectively]. A schematic of the valve operation is inserted below each panel in the first column. For abbreviations, see Fig. 1. The valve schematic inset below each panel is for visual illustrative purpose only. Video 1: Normal backward FTLE field. Multimedia view: https://doi.org/10.1063/5.0021372.1; Video 2: SLP backward FLTE field. Multimedia view: https://doi.org/10.1063/5.0021372.2; Video 3: NSLP backward FTLE field. Multimedia view: https://doi.org/10.1063/5.0021372.3; Video 4: BLP backward FTLE field. Multimedia view: https://doi.org/10.1063/5.0021372.4; Video 5: SLT backward FTLE field. Multimedia view: https://doi.org/10.1063/5.0021372.5; Video 6: NSLT backward FTLE field. Multimedia view: https://doi.org/10.1063/5.0021372.6

vortical structure is visible (see instant 1 for SLP and NSLP in Fig. 3). A series of impingement between the propagating jets and the aortic wall is shown in Videos 2 and 3 in Fig. 3 (Multimedia view). The free leaflet jet propagates faster downstream, occupying a larger area in comparison with the partially blocked side (instant 2 in SLP and NSLP). Additionally, further downstream, the vortical structures occupy larger regions when compared to the structure from the partially blocked side while both structures are approaching each other. The FTLE field shows the vortex rolling along the wall after impingement with a hook-shaped front that propagates toward the center (at instant 2). More details about the interaction of the downstream vortical structures are shown in Videos 2 and 3 in Fig. 3 (Multimedia view). At the same instant, the jet is deflected toward the wall on the free leaflet side in both cases SLP and NSLP. This jet deflection is caused by the large circulating regions downstream of the partially blocked leaflet, which pushes the propagating jet to the other side of the aorta (the free leaflet side). During the deceleration phase (at instant 4), the FTLE ridges fade and the jet boundary width (closer to the aortic root) shrinks.

When both leaflets are partially blocked, narrow FTLE ridges are noticed from the lateral jets with non-organized mushroom-like vortices (see instant 1 in Fig. 3). At instant 2, the previous vortical structures fades rapidly, while two distinguished ridges define the lateral flow jets. At peak systole (instant 3), the lateral jet boundaries

© Author(s) 2020

widen and propagate parallel to the aortic wall. During the deceleration phase, the jet boundary becomes more deflected toward the sinuses (instant 4). For the temporal evolution of the FTLE field of the BLP case, see Video 4 in Fig. 3 (Multimedia view).

By totally blocking one leaflet, clear vertical mushroom-like jet boundary structures with their side vortices are noticed at the free leaflet side. Moreover, a delayed structure appears at the location of the central jet, as shown at instant 1 in Fig. 3. By moving to instant 2, one can see a large dispersion of structures along the free leaflet side and vortical structures are observed to expand laterally toward the center close to the sinotubular junction. The vortical structures closer to the wall are squeezed, and the rolling contact between the vortices and the aortic wall induces a high deformation on the structures [see cardiac time t/T = 0.21–0.3 in Videos 5 and 6 in Fig. 3 (Multimedia view)]. At the same cardiac time in the videos, the expansion of the central vortices is due to the consecutive propagation of the jets where the central vortices are repeatedly formed and deflected toward the low dynamics regions (downstream of the blocked leaflet). At instant 3, the vortical structures stretch laterally near the exit of the ascending aorta, while a region of reversed flow is also formed. A series of mixing between the reversed flow and the central sided vortical structure is observed (see the video for SLT and NSLT during cardiac time = 0.17 s–0.41 s), where the resulting structure propagates upstream toward the aortic root. The reader is referred to Videos 5 and 6 in Fig. 3 (Multimedia view) for visual reference.

The forward FTLE fields in Fig. 4 reveal the hidden structures in the aortic flow. The distinguished FTLE ridges exist at instant 3 in SLP and NSLP where the ridges are localized at the top of the aortic section. Moreover, FTLE ridges are witnessed (with different

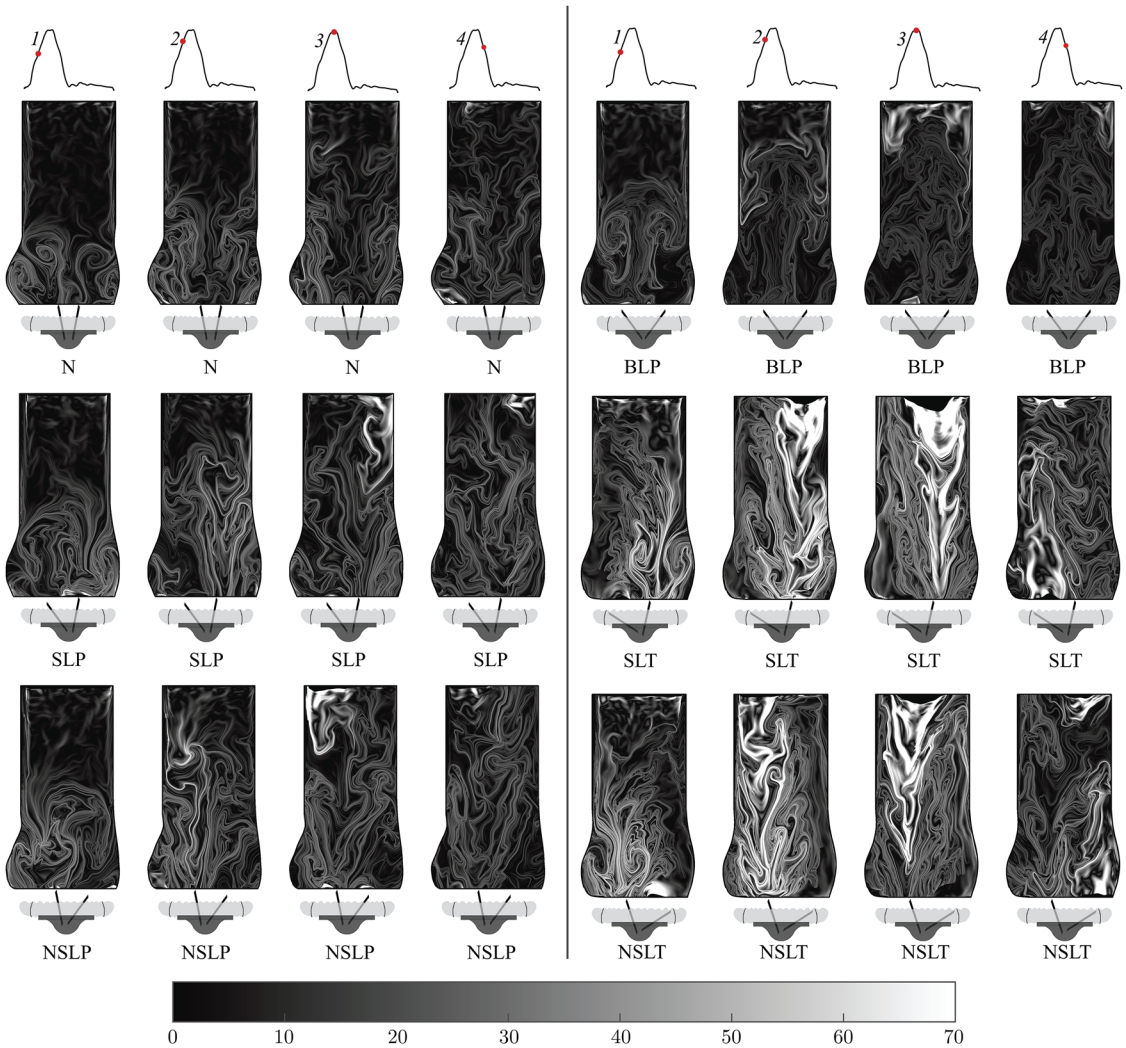

FIG. 4. Forward finite-time Lyapunov exponent field at four time instants during the systolic phase. Inset in the top row shows the location of the four time instants during the cardiac cycle. A schematic of the valve operation is inserted below each panel. For abbreviations, see Fig. 1. The valve schematic inset below each panel is for visual illustrative purpose only.

© Author(s) 2020

dispersion) in SLT and NSLT during the four reported instants. The importance of revealing repelling LCSs can be justified by the findings of Shadden and Hendabadi[34] who suggested that the platelet activation potential is maximized on repelling LCSs. The relationship between the valve dysfunction and the FTLE fields is assessed here by computing the probability density functions (PDFs) of forward-FTLE fields during the systolic phase, as shown in Fig. 5. All investigated cases have asymmetric FTLE distribution. The normal case has a narrow positively skewed distribution. Notably, the distribution broadness increases by applying valve dysfunction where the PDFs of partially blocked cases (NSLP, SLP, and BLP) are larger than that in the normal case and smaller than that in the totally blocked cases (SLT and NSLT). A similar trend between the cases is noticed in the mean value of FTLE. The PDFs of backward-FTLE fields during the systolic phase are reported in Fig. 10.

C. Lagrangian particle advection and accumulated shear stresses

As the FTLE fields reveal the barriers of many flow structures, we hypothesized that different signatures of accumulated shear stresses τ_{acc} will occur for particles released on the FTLE ridges compared to other flow locations. Therefore, we selected the FTLE field at an instant briefly after valve opening ($t/T = 0.204$) and placed particles on the locations of FTLE ridges (both forward and backward). To specify the FTLE ridges, a threshold (20% of $FTLE_{Max}$) is used for all cases. Then, equally spaced particles are advected forward in time while their corresponding τ_{acc} is computed forward in time between $t/T = 0.204$ and 0.524 and backward in time between $t/T = 0.204$ and 0. The reader is referred to Ref. 18 for details about τ_{acc} computation. The same particles are also advected backward in time to evaluate the τ_{acc} they attained before reaching the FTLE ridge. Histograms of τ_{acc} for all cases are reported in Figs. 6 and 7 corresponding to particles advected from forward and backward FTLE, respectively. Figure 6 shows that particles released on the FTLE ridges (in blue) experience more elevated and distinct levels of τ_{acc} when compared with the particles released outside the FTLE ridges. The increase in the mean value of τ_{acc} is shown using the inset in each panel of Fig. 6 where the particles in the normal case have the largest increase in the mean value of τ_{acc} with 87.5% (see Video S1 in the supplementary material). Interestingly, the lowest increase occurs in the totally blocked cases (20.2% and 25.9% for SLT and NSLT, respectively). For the temporal evolution of the τ_{acc} on the advected particles of SLT and NSLT, see Videos S2 and S3 in the supplementary material, respectively. Under partial blockage of the leaflets, the mean value of τ_{acc} increased by 22.3%, 81.0%, and 40.5% for cases BLP, SLP, and NSLP, respectively [see the temporal evolution of τ_{acc} following the same order in Videos S4, S5 and S6 in supplementary material.

Now when considering attracting LCSs, Fig. 7 shows that the particles released on the attracting LCSs (in blue) also experience more elevated levels of τ_{acc} when compared with the particles released outside the LCS regions. The particles released on the LCS vs not on the LCS in the normal case have an increase in the mean value of τ_{acc} of 80.3%. Interestingly, the lowest increase occurs in the totally blocked cases (22% and 22.9% for SLT and NSLT, respectively). Under partial blockage of the leaflets, the mean value of τ_{acc} increased by 27.2%, 86.9%, and 38.3% for cases BLP, SLP, and NSLP, respectively.

D. Spectral analysis of velocity signals

Time-frequency spectra are reported for three probed points in the flow field, which are located on the peak systolic backward FTLE field at t/T = 0.34, as shown in Fig. 8. The frequency is presented in terms of Strouhal number ($St = fD/u_m$, where f is the frequency, D is the aortic diameter, and u_m is the spatially averaged peak systolic velocity). Clearly, the normal case has dominant low frequency events at the three selected locations when compared to all dysfunctional scenarios, while merely few high frequency events are noticed at points 1 and 2. By focusing on point 3, one can notice that the flow recovered its undisturbed nature. As intuitively expected, by reducing the mobility of the leaflets, turbulence—driven by flow separation from the leaflet surface—can be identified in the high power level at the points 1 and 2 along the valve particularly for SLP, NSLP, and BLP. These high-frequency events start with the systolic phase and expand in an intermittent manner until peak systole ($0.15 < t/T < 0.35$). Shortly after peak systole, the power of high-frequency events starts fading. Remarkably, power spectra are relatively higher at the partially blocked side (point 2 and 1 in SLP

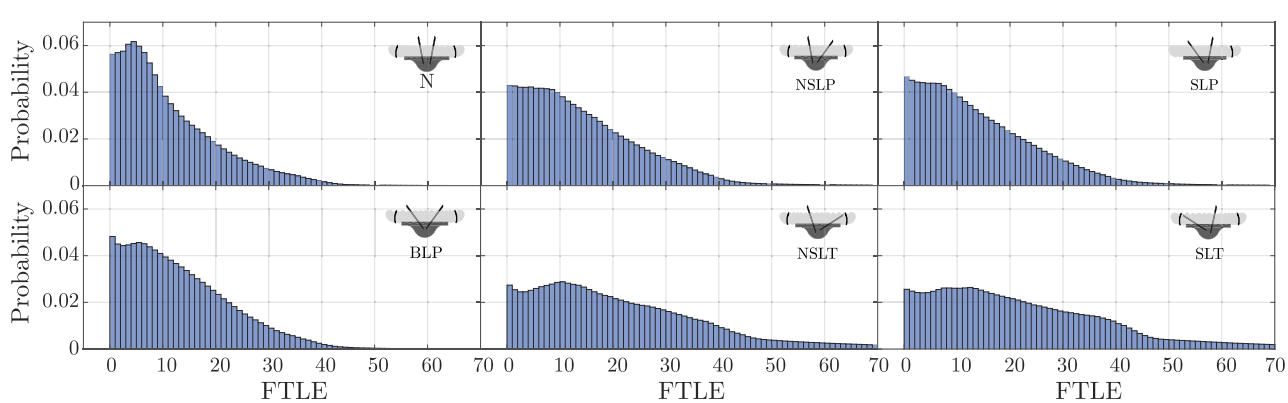

FIG. 5. Probability distribution functions of forward FTLE fields during systolic phase for all cases.

© Author(s) 2020

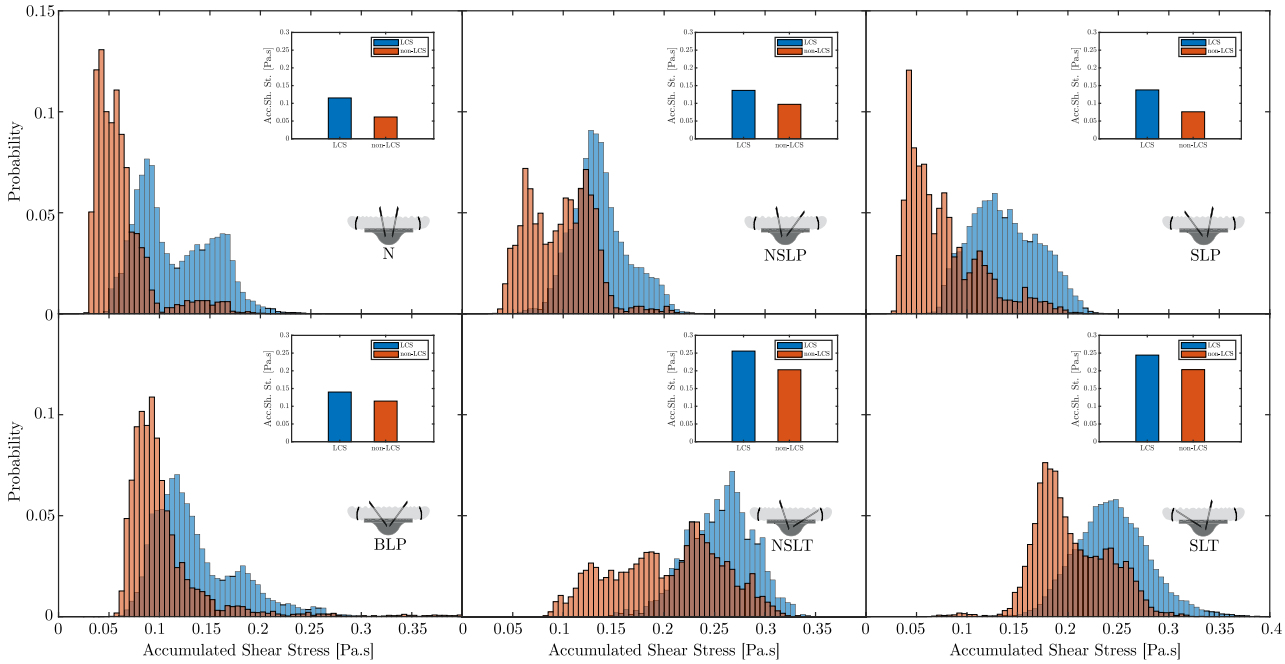

FIG. 6. Histogram of accumulated shear stress on two sets of advected particles where the blue histogram corresponds to particles located on the forward-FTLE (repelling LCS) and the red histogram corresponds to the particles released outside the repelling LCS. The inset inside each panel shows the mean value of accumulated shear stress for both histograms. For abbreviations, see Fig. 1.

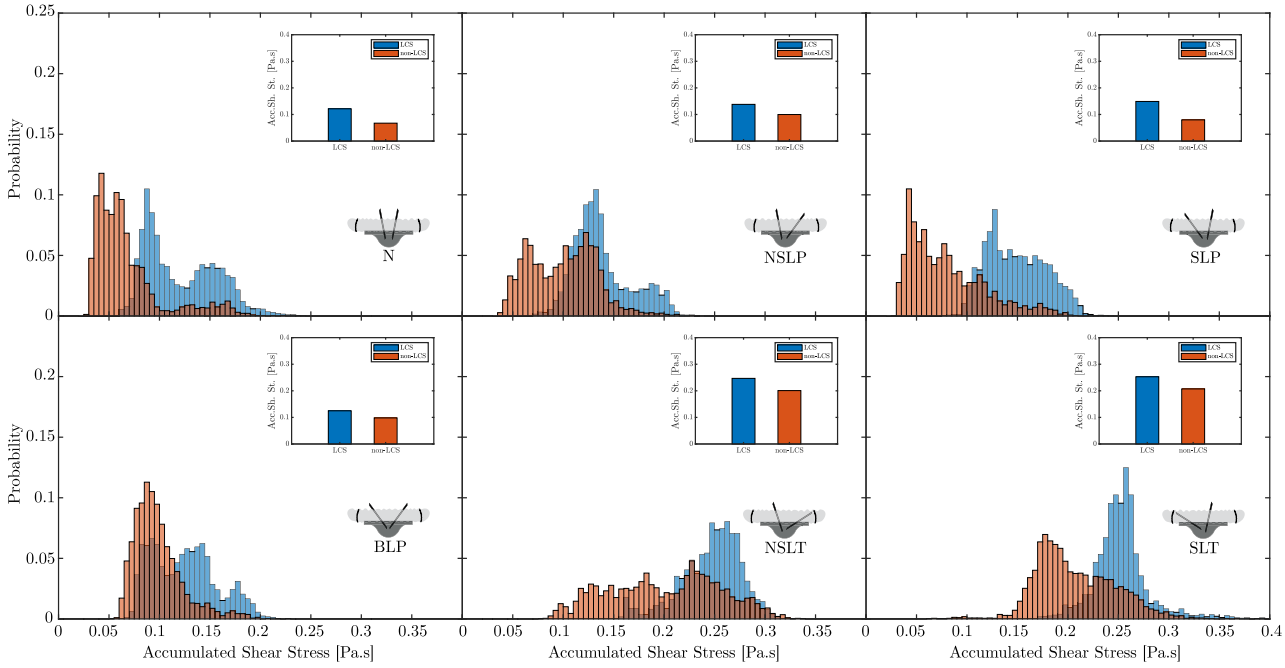

FIG. 7. Histogram of accumulated shear stress on two sets of advected particles where the blue histogram corresponds to particles located on the backward-FTLE (attracting LCSs) and the red histogram corresponds to the particles released outside the attracting LCSs. The accumulated shear stress τ_{acc} is computed up to t/T = 0.52. The inset inside each panel shows a magnified view of the histogram. For abbreviations, see Fig. 1.

© Author(s) 2020

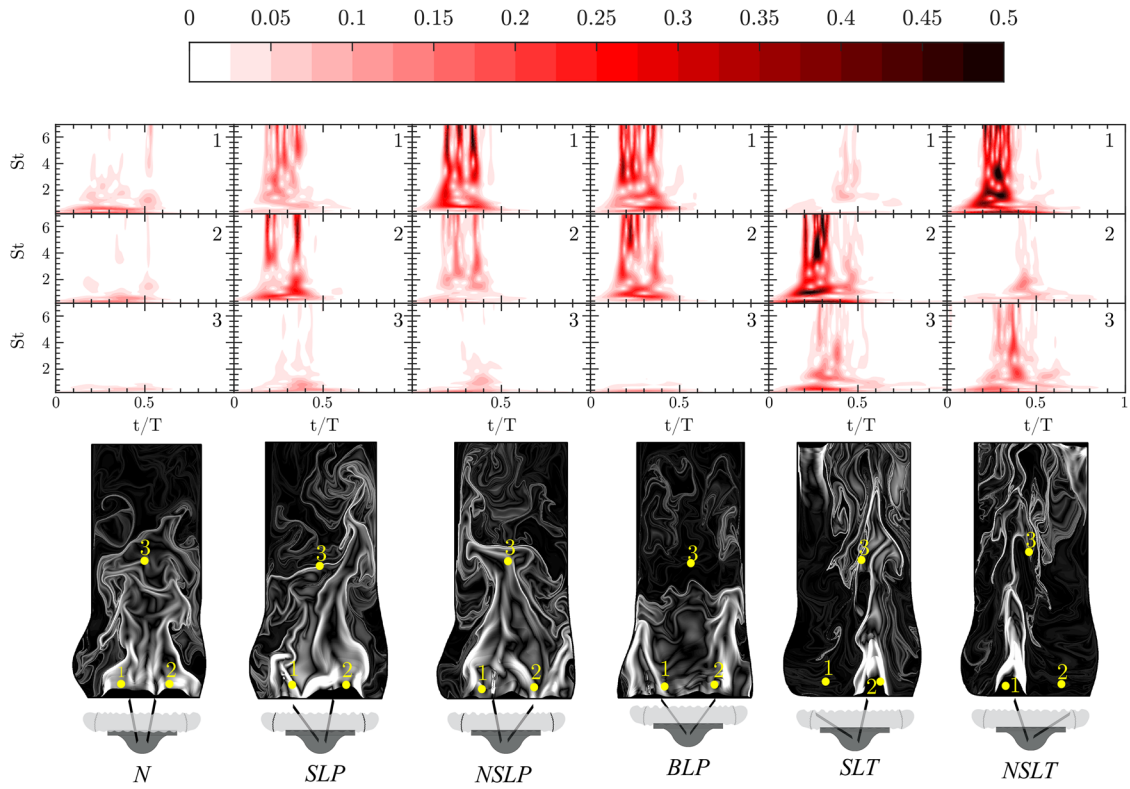

FIG. 8. Time-frequency spectra of the signal representing the v velocity component during one cardiac cycle (t/T from 0 to 1). The v velocity signal at three points downstream the valve placed on the backward FTLE fields at t/T = 0.34. For abbreviations, see Fig. 1.

and NSLP, respectively). Downstream turbulent events at point 3 are briefly noticed in SLP and NSLP around ($0.3 < t/T < 0.4$), while the flow remains undisturbed in BLP. When the leaflets are totally blocked, multiple high-frequency high-power events start with the systolic phase at $0.2 < t/T < 0.35$ at points 2 and 1 in SLT and NSLT, respectively. Notably, the points above the totally blocked leaflets experience few similar events at ($0.4 < t/T < 0.5$), which occur briefly after valve closure. This delayed series of turbulent events are caused by the recirculating flow, which has a reversed direction. The disturbance is carried downstream where high-frequency events are noticed in point 3 for SLT and NSLT. Further analysis of the time-frequency spectra is reported in Fig. 11.

IV. DISCUSSION AND CONCLUSION

One important cause of BMAV dysfunction is thrombus formation,[8,9] and PRT and PRI can then be used to examine the tendency of fluid particles to reside in the vicinity of the valve for longer times. The percentage of particles that are retained inside the aorta by the end of the second cycle has significantly increased for all cases, except for the NSLP case. In the NSLT case, we noticed that more particles are departing the domain from the valve side (upstream) driven by a strong recirculation. In fact, PRT and PRI can identify the level of flow recirculation or stagnation within the circulatory system.[38] Moreover, the value of PRI and the location of the residing particle change with the degree and orientation of the leaflet dysfunction. Therefore, certain dysfunctional cases (such as SLP, BLP, and SLT) can be linked to more serious consequences such as thromboembolism, which can cause coronary artery occlusion.[45] Lagrangian coherent structures are distinguished material lines that separate the fluid into regions with different dynamics; therefore, high levels of shear stresses along the LCS are expected. In this study, we show the attracting LCSs (backward FTLE ridges) and their ability to represent flow structures such as vortex boundaries and jet fronts. Moreover, LCSs are able to show the interaction of structures with the wall and with each other. Statistically, the PDFs of the forward FTLE field (for all cases during systole) show an asymmetric and broad pattern, which denotes a non-uniform mixing of the aortic flow.[46,47] The broader distribution of the PDFs in the partially and totally blocked cases is related to the higher strain rates[46] due to the dysfunction. In our analysis, the local maxima of the FTLE fields revealed fluid mixing geometry in the ascending aorta.[41] Moreover, the FTLE fields can provide a better understanding of the chaotic properties of fluid flow, as reported in Refs. 48 and 49 where the positive FTLE values generally indicate chaotic advection.[48]

As LCSs represent a barrier between different dynamics within the flow, the particles that are released from the LCSs therefore show a tendency to accumulate higher levels of shear stresses in comparison to the particles released elsewhere in the aorta. The

© Author(s) 2020

increase in the level of τ_{acc} between particles released from repelling LCS and elsewhere is at least 20%, which is consistent with the findings in Ref. 34. This remark can be useful in computing τ_{acc} only for particles released from the LCSs where higher values are expected. Using such evaluation for cardiac assisting devices can provide the values of τ_{acc} with a focus on the highest activated particles. The design of the devices can then be optimized accordingly. As Bluestein *et al.*[11] suggested that vortex pairing can create a large platelet aggregate, we noticed a series of vortex pairing in the time evolving FTLE fields [see Videos 1-6 in Fig. 3 (Multimedia view)]. Nevertheless, a clear demonstration of the vortex pairing is shown by adding different colors (red and green) to the released particles, which shows the interaction of the LCSs (since the particles are released from the LCSs) and the vortex pairing phenomenon. By the end of the first cardiac cycle, the aorta contains multiple vortex pairs that can be seen in cases SLP, NSLP, and BLP as in Videos S7-S9 in the supplementary material respectively. As some vortex pairs are located close to the valve, there is a high possibility of platelet deposition on the valve, which may further increase the severity of the dysfunction.[50] In the totally blocked cases (SLT and NSLT), the possible platelet aggregate has two paths, one is further downstream and the other toward the free leaflet, which can also cause a possible deposition on the valve. Such a scenario can be life-threatening.

In order to quantify the non-laminar nature of the flow downstream of the valve, we extracted three velocity signals and computed their time-frequency spectra. The degree of identified flow disturbance is minimal in the normal case, which is consistent with the findings in Refs. 51 and 52 regarding the BMAV. In all cases, the highest velocity disturbance is noticed during the systolic phase where it is likely that the flow is affected by the flow separation along the leaflet, as discussed in Refs. 11, 20, and 52. The highest level of turbulence convected downstream of the valve is noticed in NSLT and SLT cases where the high velocity penetrating jet causes a series of vortex shedding breaking the jet side into multiple small eddies that propagate further downstream of the valve (see the video that corresponds to the FTLE fields of cases SLT and NSLT). Moreover, eddies are gathering particles with a high level of accumulated shear stress, which can promote the potential of platelet aggregation.[20,53] Finally, the study elucidates the importance of performing Lagrangian analysis on the flow downstream of a BMHV, and other cardiovascular devices, where revealing the LCSs in the flow can provide a basis for the location of potentially activated platelets. This study also sheds light on the potential consequences of valve dysfunction on the level of non-laminar flow further downstream the BMAV.

V. LIMITATIONS

This study should be considered with its limitations inherent to *in vitro* measurements. First, the length between the aortic root and the ventricular outflow tract is non-anatomic, which is essential in the experiment to have a clear optical access above the aortic root. The effect of this limitation is expected to be minor since the left ventricular (LV) flow is usually laminar under healthy conditions, and the extra length will not allow the flow to fully develop before approaching the valve. Another limitation is the absence of coronary flow (4% of cardiac output), which is expected to alter the flow inside the sinus region, in particular. However, our main interest is in the main flow, which is minimally affected by the coronary flow. Despite using an elastic aortic model, the specific effect of different levels of peripheral expansion of the aorta on the downstream flow is not included in this study and can be included in future studies. The 2D planar flow measurement is a limitation itself where the flow downstream the BMAV is of complex 3D nature. Moreover, using a straight aortic model will induce changes to the downstream flow dynamics when compared with a curved ascending aorta. For instance, in the curved aorta, a helical 3D flow pattern and secondary vortical structures (owing to a high Dean number) could be noticed.[54,55] The reader is referred to Ref. 56 for more details about the effect of aortic curvature on the 2D flow pattern. Therefore, further studies could investigate the effect of valve dysfunction on a curved aortic model. To overcome this limitation, the selected plan of measurement is symmetric and matches the clinical measurement plan (in 2D studies); however, 3D measurements using tomographic PIV (for time resolved 3D flow fields) or by scanning multiple 2D planes (in the horizontal and vertical directions) are needed in the future. Such investigations can reveal the effect of leaflet orientations (with respect to the sinuses) on the reported asymmetric 3D flow field[35,57,58] along with the downstream evolution of the aortic helical flow.[54,55] Finally, the released particles are treated as massless particles, which is not the case for real blood. Numerical studies can use our results as a validation benchmark by extracting a planar slide analogous to the one investigated in this study and extend the

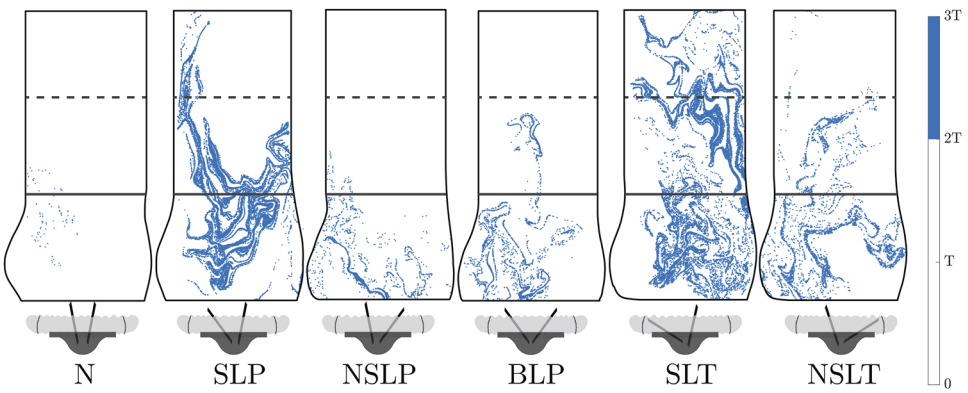

FIG. 9. Lagrangian particle residence time map showing the regions where particles reside more than two cardiac cycles (PRT > 2 T) in blue. The ascending aorta is divided into three equally spaced regions defined by the two horizontal lines (both dashed and solid). The distance between the regions correspond to one valve diameter. For abbreviations, see Fig. 1.

© Author(s) 2020

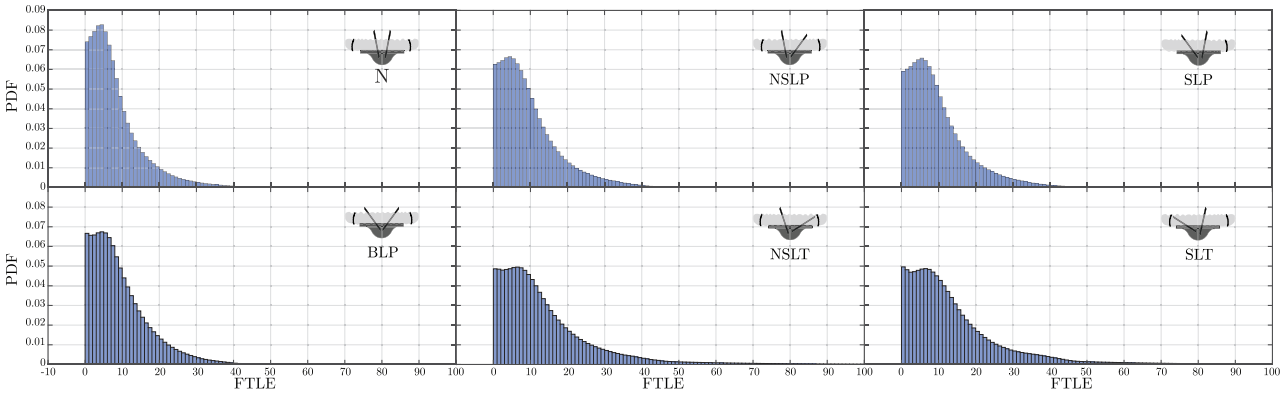

FIG. 10. Histograms of forward FTLE fields during one cardiac cycle for all cases. For abbreviations, see Fig. 1.

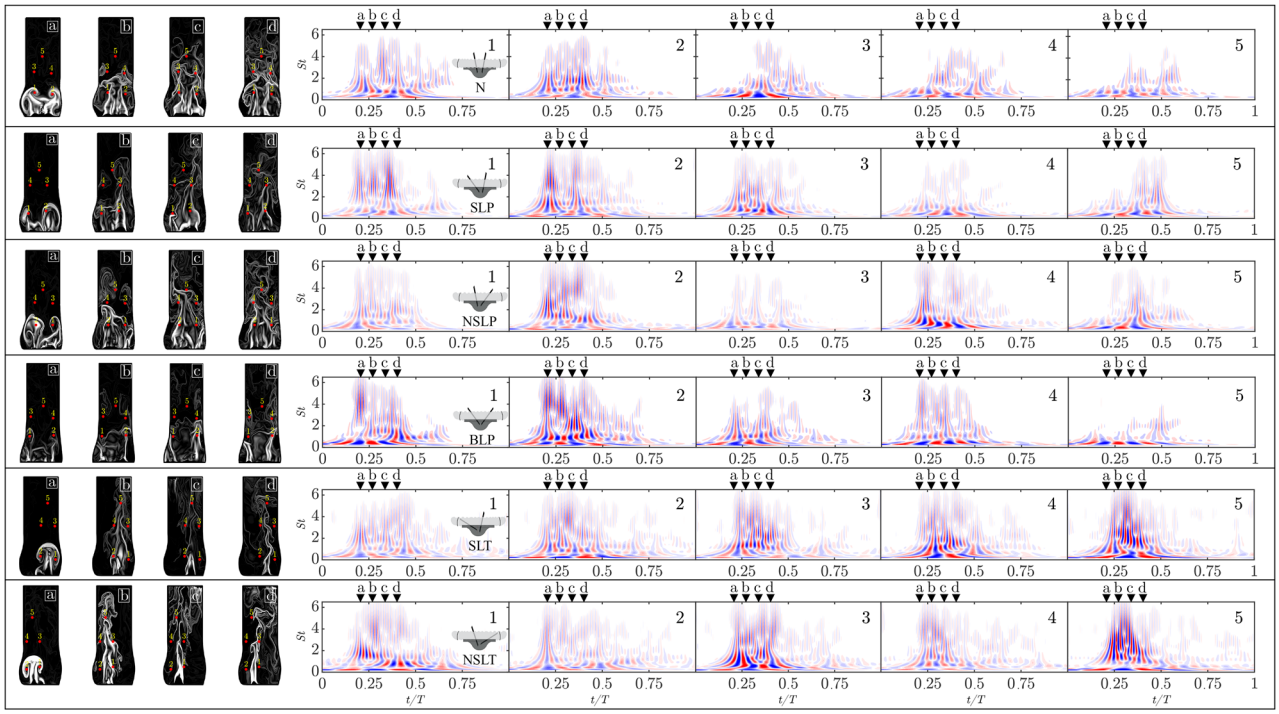

FIG. 11. Time-frequency spectra (real part) of the signal representing the v velocity component during one cardiac cycle. Each panel has four backward FTLE fields representing four time instants during the systolic phase [(a)–(d)]. Inside each FTLE field, five velocity points are precisely located and numbered from 1 to 5. The selection of the five points is based on the development of the FTLE field at instant *a*, where the first two points are at the center (or as close as possible) of the vortical structures. The remaining three points are distributed downstream of the first two points in order to capture the effect of LCS propagation. In all spectral plots, the red and blue colors identify the oscillation in the velocity signal fluctuation, while the axes specify the time and Strouhal number (*St*) at each event. In the normal case, between the axisymmetric points (1–4), a clear symmetric spectra is noticed during all instants with a clear delay of the high *St* events when moving from (1 and 2) to (3 and 4). This symmetric behavior can be deduced from the repelling LCS instants where the structures crossing at each point tend to be axisymmetric themselves. Moreover, the spectra can show the early arrival of structures to point 4 when compared with point 3. As the structures are highly deformed, a lower *St* is noticed at points 3, 4, and 5. For other cases, the delay of events noticed from points (1 and 2) to (3 and 4) is still noticeable; however, the axisymmetric spectra are only noticed in the BLP case. For other cases (SLP, NSLP, SLT, and NSLT), a clear unbalance in the LCS spatial distribution is noticed, which affects the timing/frequency of the events. For the SLT and NSLT cases, extremely high oscillations (indicating higher vortex shedding frequency) are noticed at point 5 (when compared with other cases), which suggests that the flow has not re-laminarized itself by means of mixing and diffusion of momentum. Under such flow conditions, aggregation of activated platelets and carrying them further downstream can be expected.[20,53]

© Author(s) 2020

analysis to 3D analysis including the inertial effect on the particle trajectories.

SUPPLEMENTARY MATERIAL

See the supplementary material for the temporal evolution of the accumulated shear stresses on particles released from the forward LCS (for all cases) and the particle advection mixing for cases SLP, NSLP and BLP.

ACKNOWLEDGMENTS

This work was supported by a grant from the Natural Sciences and Engineering Research Council of Canada (Grant No. 343164-07). G.D.L. was supported by the Vanier Canada Graduate Scholarship.

APPENDIX: ADDITIONAL ILLUSTRATIONS OF PRT MAPS, FORWARD FTLE FIELDS, AND TIME-FREQUENCY SPECTRA

Figure 9 shows the Lagrangian particle residence time map where particles reside more than two cardiac cycles (PRT > 2 T) are in blue. Figure 10 shows the histograms of forward FTLE fields during one cardiac cycle. Figure 11 shows the real part of the time-frequency spectra of velocity signal extracted at selected location downstream of the valve.

DATA AVAILABILITY

The data that support the findings of this study are available from the corresponding author upon reasonable request.

REFERENCES

[1] S. Saeed, M. R. Dweck, and J. Chambers, "Sex differences in aortic stenosis: From pathophysiology to treatment," Expert Rev. Cardiovasc. Ther. **18**, 65–76 (2020).
[2] J. J. Thaden, V. T. Nkomo, and M. Enriquez-Sarano, "The global burden of aortic stenosis," Prog. Cardiovasc. Dis. **56**, 565–571 (2014), part of the Special Issue: Transcatheter Aortic Valve Replacement.
[3] S. Badiani, J. van Zalen, T. A. Treibel, S. Bhattacharyya, J. C. Moon, and G. Lloyd, "Aortic stenosis, a left ventricular disease: Insights from advanced imaging," Curr. Cardiol. Rep. **18**, 80 (2016).
[4] R. A. Nishimura, C. M. Otto, R. O. Bonow, B. A. Carabello, J. P. Erwin, L. A. Fleisher, H. Jneid, M. J. Mack, C. J. McLeod, P. T. O'Gara, V. H. Rigolin, T. M. Sundt, and A. Thompson, "2017 AHA/ACC focused update of the 2014 AHA/ACC guideline for the management of patients with valvular heart disease: A report of the American college of cardiology/American heart association task force on clinical practice guidelines," Circulation **135**, e1159–e1195 (2017).
[5] J. Offstad, K. Andersen, P. Paulsson, J. Andreasson, U. Kjellman, O. Lundblad, K. G. Engstrøm, R. Haaverstad, and J. L. Svennevig, "The Scandinavian multicenter hemodynamic evaluation of the SJM Regent aortic valve," J. Cardiothorac. Surg. **6**, 163 (2011).
[6] T. Nishida, H. Sonoda, Y. Oishi, Y. Tanoue, H. Tatewaki, Y. Shiokawa, and R. Tominaga, "Long-term comparison of three types of aortic St. Jude medical mechanical prosthesis in Japanese patients," Circ. J. **79**, 2193–2200 (2015).
[7] J. P. Rose, T. L. Rihn, and S. F. Long, "Warfarin sensitivity after mechanical heart valve replacement," Pharmacotherapy **18**, 856–859 (1998).
[8] R. Roudaut, K. Serri, and S. Lafitte, "Thrombosis of prosthetic heart valves: Diagnosis and therapeutic considerations," Heart **93**, 137–142 (2007).
[9] W. Ma, B. Hou, A. Abdurusul, D. Gong, Y. Tang, Q. Chang, J. Xu, and H. Sun, "Dysfunction of mechanical heart valve prosthesis: Experience with surgical management in 48 patients," J. Thorac. Dis. **7**, 2321–2329 (2015).
[10] J. Barbetseas, S. F. Nagueh, C. Pitsavos, P. K. Toutouzas, M. A. Quiñones, and W. A. Zoghbi, "Differentiating thrombus from pannus formation in obstructed mechanical prosthetic valves: An evaluation of clinical, transthoracic and transesophageal echocardiographic parameters," J. Am. Coll. Cardiol. **32**, 1410–1417 (1998).
[11] D. Bluestein, E. Rambod, and M. Gharib, "Vortex shedding as a mechanism for free emboli formation in mechanical heart valves," J. Biomech. Eng. **122**, 125–134 (2000).
[12] O. Smadi, I. Hassan, P. Pibarot, and L. Kadem, "Numerical and experimental investigations of pulsatile blood flow pattern through a dysfunctional mechanical heart valve," J. Biomech. **43**, 1565–1572 (2010).
[13] S. Shahriari, H. Maleki, I. Hassan, and L. Kadem, "Evaluation of shear stress accumulation on blood components in normal and dysfunctional bileaflet mechanical heart valves using smoothed particle hydrodynamics," J. Biomech. **45**, 2637–2644 (2012).
[14] O. Smadi, J. Garcia, P. Pibarot, E. Gaillard, I. Hassan, and L. Kadem, "Accuracy of Doppler-echocardiographic parameters for the detection of aortic bileaflet mechanical prosthetic valve dysfunction," Eur. Heart J.: Cardiovasc. Imaging **15**, 142–151 (2014).
[15] F. Sotiropoulos, T. B. Le, and A. Gilmanov, "Fluid mechanics of heart valves and their replacements," Annu. Rev. Fluid Mech. **48**, 259–283 (2016).
[16] L. Haya and S. Tavoularis, "Effects of bileaflet mechanical heart valve orientation on fluid stresses and coronary flow," J. Fluid Mech. **806**, 129–164 (2016).
[17] F. M. Susin, S. Espa, R. Toninato, S. Fortini, and G. Querzoli, "Integrated strategy for *in vitro* characterization of a bileaflet mechanical aortic valve," BioMed. Eng. OnLine **16**, 29 (2017).
[18] A. Darwish, G. Di Labbio, W. Saleh, O. Smadi, and L. Kadem, "Experimental investigation of the flow downstream of a dysfunctional bileaflet mechanical aortic valve," Artif. Organs **43**, E249 (2019).
[19] C. D. Winant and F. K. Browand, "Vortex pairing: The mechanism of turbulent mixing-layer growth at moderate Reynolds number," J. Fluid Mech. **63**, 237–255 (1974).
[20] D. Bluestein, Y. M. Li, and I. B. Krukenkamp, "Free emboli formation in the wake of bi-leaflet mechanical heart valves and the effects of implantation techniques," J. Biomech. **35**, 1533–1540 (2002).
[21] B. Min Yun, C. K. Aidun, and A. P. Yoganathan, "Blood damage through a bileaflet mechanical heart valve: A quantitative computational study using a multiscale suspension flow solver," J. Biomech. Eng. **136**, 101009 (2014).
[22] R. Cucitore, M. Quadrio, and A. Baron, "On the effectiveness and limitations of local criteria for the identification of a vortex," Eur. J. Mech. B: Fluids **18**, 261–282 (1999).
[23] A. Provenzale, "Transport by coherent barotropic vortices," Annu. Rev. Fluid Mech. **31**, 55–93 (1999).
[24] S. C. Shadden and C. A. Taylor, "Characterization of coherent structures in the cardiovascular system," Ann. Biomed. Eng. **36**, 1152–1162 (2008).
[25] S. C. Shadden and A. Arzani, "Lagrangian postprocessing of computational hemodynamics," Ann. Biomed. Eng. **43**, 41–58 (2015).
[26] M. G. Badas, F. Domenichini, and G. Querzoli, "Quantification of the blood mixing in the left ventricle using Finite Time Lyapunov xponents," Meccanica **52**, 529–544 (2017).
[27] G. Di Labbio and L. Kadem, "Jet collisions and vortex reversal in the human left ventricle," J. Biomech. **78**, 155–160 (2018).
[28] A. Olcay, A. Amindari, K. Kirkkopru, and H. Yalcin, "Characterization of disturbed hemodynamics due to stenosed aortic jets with a Lagrangian coherent structures technique," J. Appl. Fluid Mech. **11**, 375–384 (2018).
[29] F. Joly, G. Soulez, D. Garcia, S. Lessard, and C. Kauffmann, "Flow stagnation volume and abdominal aortic aneurysm growth: Insights from patient-specific computational flow dynamics of Lagrangian-coherent structures," Comput. Biology Med. **92**, 98–109 (2018).
[30] O. Mutlu, A. B. Olcay, C. Bilgin, and B. Hakyemez, "Evaluating the effectiveness of 2 different flow diverter stents based on the stagnation region formation in an

© Author(s) 2020

aneurysm sac using Lagrangian coherent structure," World Neurosurg. **127**, e727–e737 (2019).
[31] S. C. Shadden, M. Astorino, and J.-F. Gerbeau, "Computational analysis of an aortic valve jet with Lagrangian coherent structures," Chaos **20**, 017512 (2010).
[32] A. Arzani and S. C. Shadden, "Characterization of the transport topology in patient-specific abdominal aortic aneurysm models," Phys. Fluids **24**, 081901 (2012).
[33] G. Di Labbio, J. Vétel, and L. Kadem, "Material transport in the left ventricle with aortic valve regurgitation," Phys. Rev. Fluids **3**, 113101 (2018).
[34] S. C. Shadden and S. Hendabadi, "Potential fluid mechanic pathways of platelet activation," Biomech. Model. Mechanobiol. **12**, 467–474 (2013).
[35] P. Miron, J. Vétel, and A. Garon, "On the use of the finite-time Lyapunov exponent to reveal complex flow physics in the wake of a mechanical valve," Exp. Fluids **55**, 1814 (2014).
[36] I. Borazjani and F. Sotiropoulos, "The effect of implantation orientation of a bileaflet mechanical heart valve on kinematics and hemodynamics in an anatomic aorta," J. Biomech. Eng. **132**, 111005 (2010).
[37] M. Raffel, C. E. Willert, S. T. Wereley, and J. Kompenhans, *Particle Image Velocimetry* (Springer Berlin Heidelberg, 2007).
[38] G.-Y. Suh, A. S. Les, A. S. Tenforde, S. C. Shadden, R. L. Spilker, J. J. Yeung, C. P. Cheng, R. J. Herfkens, R. L. Dalman, and C. A. Taylor, "Quantification of particle residence time in abdominal aortic aneurysms using magnetic resonance imaging and computational fluid dynamics," Ann. Biomed. Eng. **39**, 864–883 (2011).
[39] G. Haller, "Distinguished material surfaces and coherent structures in three-dimensional fluid flows," Physica D **149**, 248–277 (2001).
[40] G. Haller, "A variational theory of hyperbolic Lagrangian coherent structures," Physica D **240**, 574–598 (2011).
[41] S. C. Shadden, F. Lekien, and J. E. Marsden, "Definition and properties of Lagrangian coherent structures from finite-time Lyapunov exponents in two-dimensional aperiodic flows," Physica D **212**, 271–304 (2005).
[42] P. C. du Toit and J. E. Marsden, "Horseshoes in hurricanes," J. Fixed Point Theory Appl. **7**, 351–384 (2010).
[43] M. Farge, "Wavelet transforms and their applications to turbulence," Annu. Rev. Fluid Mech. **24**, 395–457 (1992).
[44] A. B. Olcay and P. S. Krueger, "Measurement of ambient fluid entrainment during laminar vortex ring formation," Exp. Fluids **44**, 235–247 (2007).
[45] P. Bruno, M. Massetti, G. Babatasi, and A. Khayat, "Catastrophic consequences of a free floating thrombus in ascending aorta," Eur. J. Cardiothorac. Surg. **19**, 99–101 (2001).
[46] D. W. Waugh and E. R. Abraham, "Stirring in the global surface ocean," Geophys. Res. Lett. **35**, L20605, https://doi.org/10.1029/2008gl035526 (2008).
[47] F. J. Beron-Vera, M. J. Olascoaga, and G. J. Goni, "Surface ocean mixing inferred from different multisatellite altimetry measurements," J. Phys. Oceanogr. **40**, 2466–2480 (2010).
[48] R. T. Pierrehumbert, "Large-scale horizontal mixing in planetary atmospheres," Phys. Fluids A **3**, 1250–1260 (1991).
[49] S. Boatto and R. T. Pierrehumbert, "Dynamics of a passive tracer in a velocity field of four identical point vortices," J. Fluid Mech. **394**, 137–174 (1999).
[50] M. Bonou, K. Lampropoulos, and J. Barbetseas, "Prosthetic heart valve obstruction: Thrombolysis or surgical treatment?," Eur. Heart J. **1**, 122–127 (2012).
[51] J. S. Liu, P. C. Lu, and S. H. Chu, "Turbulence characteristics downstream of bileaflet aortic valve prostheses," J. Biomech. Eng. **122**, 118–124 (2000).
[52] A. P. Yoganathan, K. B. Chandran, and F. Sotiropoulos, "Flow in prosthetic heart valves: State-of-the-art and future directions," Ann. Biomed. Eng. **33**, 1689–1694 (2005).
[53] Z. J. Huang, C. L. Merkle, S. Abdallah, and J. M. Tarbell, "Numerical simulation of unsteady laminar flow through a tilting disk heart valve: Prediction of vortex shedding," J. Biomech. **27**, 391–402 (1994).
[54] M. Markl, P. J. Kilner, and T. Ebbers, "Comprehensive 4D velocity mapping of the heart and great vessels by cardiovascular magnetic resonance," J. Cardiovasc. Magn. Reson. **13**, 7 (2011).
[55] H. G. Bogren, M. H. Buonocore, and R. J. Valente, "Four-dimensional magnetic resonance velocity mapping of blood flow patterns in the aorta in patients with atherosclerotic coronary artery disease compared to age-matched normal subjects," J. Magn. Reson. Imaging **19**, 417–427 (2004).
[56] L. Haya and S. Tavoularis, "Comparison of *in vitro* flows past a mechanical heart valve in anatomical and axisymmetric aorta models," Exp. Fluids **58**, 73 (2017).
[57] C. Brücker, "Dual-camera DPIV for flow studies past artificial heart valves," Exp. Fluids **22**, 496–506 (1997).
[58] M. D. D. Tullio, A. Cristallo, E. Balaras, and R. Verzicco, "Direct numerical simulation of the pulsatile flow through an aortic bileaflet mechanical heart valve," J. Fluid Mech. **622**, 259–290 (2009).

© Author(s) 2020